

PROBING PARTICLE ACCELERATION THROUGH BROADBAND EARLY AFTERGLOW EMISSION OF MAGIC GAMMA-RAY BURST GRB 190114C

KATSUAKI ASANO¹, KOHTA MURASE^{2,3,4,5}, AND KENJI TOMA^{6,7}

¹Institute for Cosmic Ray Research, The University of Tokyo, 5-1-5 Kashiwanoha, Kashiwa, Chiba 277-8582, Japan; asanok@icrr.u-tokyo.ac.jp

²Department of Physics, The Pennsylvania State University, University Park, Pennsylvania 16802, USA

³Department of Astronomy & Astrophysics, The Pennsylvania State University, University Park, Pennsylvania 16802, USA

⁴Center for Multimessenger Astrophysics, Institute for Gravitation and the Cosmos, The Pennsylvania State University, University Park, Pennsylvania 16802, USA

⁵Center for Gravitational Physics, Yukawa Institute for Theoretical Physics, Kyoto University, Kyoto 606-8502, Japan

⁶Frontier Research Institute for Interdisciplinary Sciences, Tohoku University, Sendai 980-8578, Japan and

⁷Astronomical Institute, Graduate School of Science, Tohoku University, Sendai 980-8578, Japan

(Dated: Submitted; accepted)
Draft version November 25, 2020

ABSTRACT

Major Atmospheric Gamma Imaging Cherenkov Telescopes (MAGIC) detected the gamma-ray afterglow of GRB 190114C, which can constrain microscopic parameters of the shock-heated plasma emitting non-thermal emission. Focusing on the early afterglow of this event, we numerically simulate the spectrum and multi-wavelength light curves with constant and wind-like circumstellar medium using a time-dependent code. Our results show that the electron acceleration timescale at the highest energies is likely shorter than 20 times the gyroperiod to reproduce the GeV gamma-ray flux and its spectral index reported by *Fermi*. This gives an interesting constraint on the acceleration efficiency for Weibel-mediated shocks. We also constrain the number fraction of non-thermal electrons f_e , and the temperature of the thermal electrons. The early optical emission can be explained by the thermal synchrotron emission with $f_e \lesssim 0.01$. On the other hand, the X-ray light curves restrict efficient energy transfer from protons to the thermal electrons, and $f_e \sim 1$ is required if the energy fraction of the thermal electrons is larger than $\sim 10\%$. The parameter constraints obtained in this work give important clues to probing plasma physics with relativistic shocks.

Subject headings: acceleration of particles — gamma-rays: bursts — radiation mechanisms: non-thermal

1. INTRODUCTION

Gamma-ray burst (GRB) 190114C at redshift $z = 0.4245$ is the first gamma-ray burst detected with imaging atmospheric Cherenkov telescopes (IACTs). MAGIC Collaboration (2019) reported gamma-ray detection in the energy range of 0.2–1 TeV from 62 s to 2454 s after the trigger by the *Swift*-BAT. The spectral component in this energy range is naturally interpreted as the synchrotron self-Compton (SSC) emission from the afterglow caused by electrons accelerated at a blastwave (MAGIC Collaboration, et al. 2019, hereafter, MAGIC-MWL paper), because the photon energy is significantly larger than the maximum photon energy expected by synchrotron radiation (see also the case in GRB 130427A, Ackermann et al. 2014). The SSC interpretation has been supported by Derishev & Piran (2019); Fraija et al. (2019); Wang et al. (2019); Zhang et al. (2020).

The SSC component in the early afterglow uniquely provides the physical information of the external shock in the early stage (see §3). In this paper, adopting the time-dependent code in Fukushima et al. (2017), we simulate the broadband emission of the afterglow in GRB 190114C. We focus on the microscopic parameters for the particle-acceleration in the relativistic shock, especially the particle acceleration timescale, the number fraction of the accelerated electrons, and the temperature of the thermal electrons. Although many studies

on this topic have discussed from a theoretical point of view (e.g., Spitkovsky 2008; Lemoine & Pelletier 2011; Sironi & Spitkovsky 2011; Sironi et al. 2013; Kumar et al. 2015), the particle-acceleration process and energy transfer from protons to electrons in GRB afterglows are not understood yet. The multi-wavelength observations of GRB 190114C afterglow can bring us hints for the acceleration mechanism.

In §2, we explain our numerical method, and review the parameter degeneracy in the afterglow modeling in §3. We show our results for spectrum and light curves in §4. In §5, we discuss thermal synchrotron emission in the early afterglow, from which we can constrain the heating efficiency of the thermal electrons or the number fraction of accelerated electrons. §6 is devoted to summary.

2. NUMERICAL METHODS

The afterglow emission is typically attributed to radiation from a shocked shell relativistically propagating in the circumstellar medium (external forward shock emission). Electrons accelerated at the shock (non-thermal electrons) emit synchrotron photons in a magnetic field amplified in the downstream. The non-thermal electrons up-scatter such synchrotron photons as well, and this process is called SSC emission. In this paper, the temporal evolution of the afterglow emission by the above two processes is calculated as follows.

2.1. Method I: Time-Dependent Calculations

We primarily adopt the numerical code in Fukushima et al. (2017) (hereafter F17). The code follows the temporal evolutions of the bulk motion of the shocked-shell, magnetic field, and electron and photon energy distributions in the shell. The shell is assumed homogeneous within the shell width ΔR . Physical processes addressed in the code are photon production and particle cooling by synchrotron and inverse-Compton with the Klein–Nishina effect, photon absorption by synchrotron self-absorption and $\gamma\gamma \rightarrow e^+e^-$ pair production, secondary pair injection, adiabatic cooling, and photon escape from the shell. Integrating the escaped photons over the shell surface, we obtain the spectral evolution for an observer with effects of the Doppler beaming and the curvature of the emission surface to address the photon arrival time.

Given the density of the circumstellar medium n and the the bulk Lorentz factor of the shell $\Gamma = 1/\sqrt{1 - \beta_{\text{sh}}^2}$ at a radius R , we can follow the evolution of the shell mass with

$$\dot{M} = 4\pi R^2 c \beta_{\text{sh}} n m_{\text{p}}. \quad (1)$$

The shock jump condition provides the energy injection into the shell. The total energy in the shell frame E'_{sh} evolves with the mass loading, radiative cooling, and adiabatic cooling. The evolution of Γ is calculated from the energy conservation

$$\Gamma E'_{\text{sh}} = E_0 + Mc^2 - E_{\text{rad}}, \quad (2)$$

where E_0 is the total energy initially released, and E_{rad} is the energy escaped from the shell as radiation.

In each time step, we add magnetic energy by assuming that the energy fraction ϵ_B of the downstream dissipated energy is converted into magnetic energy. The energy distribution of non-thermal electrons at injection is estimated by using the standard parameters: the energy fraction ϵ_e , and the number fraction f_e (see F17 for details). The injection spectrum is assumed as a single power-law with an index p , minimum Lorentz factor γ_{m} , and an exponential cutoff at γ_{max} . The value of γ_{max} is obtained from the balance between the acceleration time and cooling time as $\eta \gamma_{\text{max}} m_e c / (eB) = t_c$, where $\eta \geq 1$ is the acceleration efficiency parameter, and t_c is the cooling time due to synchrotron and inverse-Compton processes. Neglecting the inverse-Compton cooling with the simple approximation $B^2 / (8\pi) = 4\Gamma^2 n m_{\text{p}} c^2 \epsilon_B$, the maximum Lorentz factor is approximated to be

$$\gamma_{\text{max}} \approx \left(\frac{\pi}{2\epsilon_B n m_{\text{p}}} \right)^{1/4} \left(\frac{3e}{2\eta \Gamma c \sigma_{\text{T}}} \right)^{1/2}. \quad (3)$$

The minimum Lorentz factor γ_{m} is numerically estimated, taking into account γ_{max} . In the limit of $\gamma_{\text{max}} \rightarrow \infty$, we obtain the well-known formula

$$\gamma_{\text{m}} \approx \frac{\epsilon_e p - 2}{f_e p - 1} (\Gamma - 1) \frac{m_{\text{p}}}{m_e}. \quad (4)$$

Given the electron injection spectrum $\dot{N}_{\text{e}}^{\text{inj}}(\gamma_e)$, our numerical code follows the temporal evolutions of the energy distributions for electrons,

$$\frac{\partial N_{\text{e}}}{\partial t} = \frac{\partial}{\partial \gamma_e} [(\dot{\gamma}_{\text{syn}} + \dot{\gamma}_{\text{IC}} + \dot{\gamma}_{\text{ad}} - \dot{\gamma}_{\text{SSA}}) N_{\text{e}}(\gamma_e)] + \dot{N}_{\text{e}}^{\gamma\gamma} + \dot{N}_{\text{e}}^{\text{inj}}, \quad (5)$$

and for photons,

$$\frac{\partial N_{\gamma}}{\partial t} = \dot{N}_{\gamma}^{\text{syn}} + \dot{N}_{\gamma}^{\text{IC}} - \dot{N}_{\gamma}^{\gamma\gamma} - \dot{N}_{\gamma}^{\text{SSA}} - \dot{N}_{\gamma}^{\text{esc}}, \quad (6)$$

in the shell, where $\dot{\gamma} > 0$ and $\dot{N} > 0$ are the energy loss/gain rate normalized by the electron mass and creation/annihilation rate, respectively, for electrons (denoted with subscript e) and photons (subscript γ). The superscripts, syn, IC, ad, SSA, $\gamma\gamma$, and esc, express the contributions due to synchrotron emission, inverse-Compton emission, adiabatic cooling, synchrotron self-absorption, electron–positron pair creation, and photon escape, respectively. From the density obtained from the jump condition and total mass, we obtain the shell volume V and the width as $\Delta R = V / (4\pi R^2)$. Then, the photon escape rate is calculated as

$$\dot{N}_{\gamma}^{\text{esc}} = \frac{c}{2W} N_{\gamma}. \quad (7)$$

For electrons, we do not incorporate the escape effect, because the mean free path is much shorter than the shell width as will be discussed in §4. Alternatively, adiabatic cooling leads to a similar effect to the escape effect. The details of other terms in Equations (5) and (6) are explained in Fukushima et al. (2017).

The electron energy distribution with the radiative cooling effect can be approximated by a broken power-law (Mészáros & Rees 1997; Sari et al. 1998); the electron spectrum has a low-energy cutoff at $\min(\gamma_{\text{m}}, \gamma_{\text{c}})$ and break at $\max(\gamma_{\text{m}}, \gamma_{\text{c}})$, where γ_{c} corresponds to the cooling energy determined by equality for the elapsed time and t_c . In the broken power-law approximation, the spectral index above the break is $p + 1$, while the low-energy index is 2 for $\gamma_{\text{m}} > \gamma_{\text{c}}$ or p for $\gamma_{\text{m}} < \gamma_{\text{c}}$. As shown in F17, our time-dependent numerical code yields a smoothly curved electron spectrum. The resultant photon spectrum also shows a smoothly curved feature. As a result, the different spectral shape around the spectral peak leads to a different parameter set from that with the conventional broken power-law approximation.

The flux obtained by this code can be different from the conventional analytical approximation by a factor of two to three (F17). The flux difference comes from the exact treatment in estimates of γ_{max} and γ_{m} , the curved electron spectrum, the flux estimate taking into account the equivalent arrival time surface, and the time-dependent treatment with the effects of the adiabatic cooling and inverse-Compton cooling. As will be shown below, a larger ϵ_B compared to that in MAGIC-MWL paper is required in our calculation.

2.2. Method II: Single-Zone Quasi-Steady Calculations

In this work, we examine the results by an independent method, using another numerical code in Murase et al. (2011) (hereafter M11) with some modifications (see also Zhang et al. 2020b, for details). In this method, we assume that the non-thermal electron distribution follows a power law. In the fast cooling regime ($\gamma_{\text{c}} < \gamma_{\text{m}}$), the steady-state electron distribution is used, which is given by

$$\frac{dN_{\text{e}}}{d\gamma_e} = \frac{t_c}{\gamma_e} \int_{\gamma_e} d\gamma'_e \frac{d\dot{N}_{\text{e}}^{\text{inj}}}{d\gamma'_e}, \quad (8)$$

where \dot{N}_e^{inj} is the injection rate of non-thermal electrons. In the slow-cooling case, we interpolate the injection spectrum and steady-state spectrum for $\gamma_m < \gamma_e < \gamma_c$. For dynamics, we use the Blandford–McKee solution with $R \approx 4\Gamma^2 ct_{\text{obs}}/(1+z)$, and the results by this method agree with the analytical results (Sari et al. 1998). Compared with the results by F17, we find that the results are in agreement within a factor of two to three.

One of the main differences comes from the fact that the single radiation zone is assumed without the integration over the equivalent time-arrival surface. There are other two notable differences. At low energies, heating due to the synchrotron self-absorption process can enhance the optical flux. In the GeV band, electromagnetics cascades can fill the dip between synchrotron and SSC components.

3. REMARKS ON THE PARAMETER DEGENERACY

Before showing our numerical results, we review the parameter degeneracy in the afterglow modeling. The evolution of the bulk Lorentz factor Γ is determined by the total energy E_0 and the density of the circumstellar medium; the constant density n_0 or the wind profile $n \propto AR^{-2}$. However, as long as E_0/n_0 or E_0/A is the same, different values of E_0 lead to the same evolution of Γ (Blandford & McKee 1976).

By adjusting the microscopic parameters, f_e , ϵ_e , and ϵ_B , we can obtain the same evolutions of the electron injection rate, γ_m , and the magnetic field B , for a different value of E_0 (Eichler & Waxman 2005). Even if we obtain all the four spectral parameters, ε_a , ε_m , ε_c , and F_{max} (break energies due to synchrotron self-absorption, γ_m , and γ_c , and the peak flux, respectively; Sari et al. 1998) at a certain observation time, we cannot determine all the five model parameters, E_0 , n_0 (or A), ϵ_e , ϵ_B , and f_e ¹.

In other words, though we cannot determine the property of the “thermal” electrons, whose number fraction is $1 - f_e$, all the four practical parameters to yield the non-thermal emission, the number of non-thermal electrons, γ_m , γ_c , and B , can be uniquely determined by the observed synchrotron spectrum in an ideal case. If we know all the four parameters above, inverse-Compton emission can be automatically calculated without ambiguity in a single-zone model². The inverse-Compton spectrum does not provide additional information for the non-thermal electrons. The parameter degeneracy is not solved by a detection of the inverse-Compton component.

However, in the very early stage, all the four spectral parameters for the synchrotron component, especially ε_a , are rarely constrained. Since the spectral parameters evolve monotonically in the standard afterglow model, ε_a is usually extrapolated from radio observations in the late stage (see e.g., Panaitescu & Kumar 2001). However, the spectral evolution can be affected by the jet break in the late stage, and radio observations for some GRB samples have shown inconsistent behavior with the standard afterglow model (Kangas & Fruchter 2001). The inconsistency may be resolved by the temporal evolutions of the

microscopic parameters, ϵ_e , ϵ_B , and f_e (Ioka et al. 2006; Maselli et al. 2014). Even for GRB 190114C, Misra et al. (2019) claimed that a model with the evolving microscopic parameters agrees with their long-term radio/mm observations.

If we assume constant values for the microscopic parameters, we should focus on the spectrum in a limited time interval rather than the entire spectral evolution. Therefore, the inverse-Compton component provides a unique information constraining the model parameters in the very early stage of an afterglow not using the observational data in the late stage.

Though the parameters degenerate with f_e , common values of $E_0 f_e$, $n_0 f_e$ (or $A f_e$), ϵ_e/f_e , and ϵ_B/f_e yield an identical model for different values of f_e . While the possible constraint on f_e will be discussed in section 5, we fix f_e as 0.3 in our calculation with F17, which provides a reasonable value for E_0 .

We also have an additional microscopic parameter η , which adjusts the maximum energy of accelerated electrons. Particle-in-cell (PIC) simulations (e.g., Sironi et al. 2013) show that the particle acceleration at a relativistic shock is a diffusive process, in which $\gamma_{\text{max}} \propto t^{1/2}$. The simulation results imply $\eta \approx r_L/\lambda_{\text{min}}$, where r_L is the particle’s Larmor radius, and λ_{min} is the minimum wavelength of plasma turbulence. In this paper, we will constrain the value of η with our numerical models, and discuss the consistency with the PIC simulation result.

4. AFTERGLOW SPECTRUM AND LIGHT CURVES

Focusing on the first ~ 1000 s, we show two models of the GRB 190114C afterglow emission: the constant circumstellar medium (ISM model) and the wind-like circumstellar medium (wind model). In Table 1, we summarize the model parameters for the two models, respectively.

As mentioned in the previous section, we adopt $f_e = 0.3$, which yields $E_0 \simeq 10^{54} (f_e/0.3)^{-1}$ erg in our modeling. This value is reasonably larger than the prompt gamma-ray energy 2.5×10^{53} erg.

The optical flux at $t_{\text{obs}} \sim 60$ s detected with *Swift*/UVOT is too bright to be explained by the forward shock emission. So the optical emission at this stage may be dominated by the reverse-shock component, emission from a shock propagating inside the ejecta coming from the central engine. As this component contributes as seed photons for inverse-Compton scattering, we take into account the reverse-shock component by manually adding a photon field in the shocked shell. The spectrum of the reverse-shock component is assumed to be the Band function (Band et al. 1993) with the low-energy index $\alpha = -1$ and high-energy index $\beta = -2.5$. The peak energy for the Band function is adjusted as $\sim 10^{-2}$ eV in the shell rest frame to reproduce the optical observation.

4.1. ISM Model

In Figure 1, we plot the evolutions of Γ and B versus time t in the central engine rest frame for the ISM model. The deceleration time, from which the shock starts to

¹ The injection index p is directly obtained from the photon spectral shape in ideal cases.

² In a multi-zone model, the time differences between the emission and scattering events can play an important role in the light curve (see e.g., Murase et al. 2011; Chen et al. 2011).

TABLE 1
 MODEL PARAMETERS

Model	E_0 [erg]	Γ_0	n_0 [cm $^{-3}$]	A	p	ϵ_e	ϵ_B	f_e
ISM (method I)	10^{54}	600	1.0	—	2.3	0.06	9.0×10^{-4}	0.3
Wind (method I)	10^{54}	300	—	0.1	2.35	0.08	1.2×10^{-3}	0.3
ISM (method II)	4×10^{53}	—	0.3	—	2.3	0.1	1.0×10^{-3}	1.0

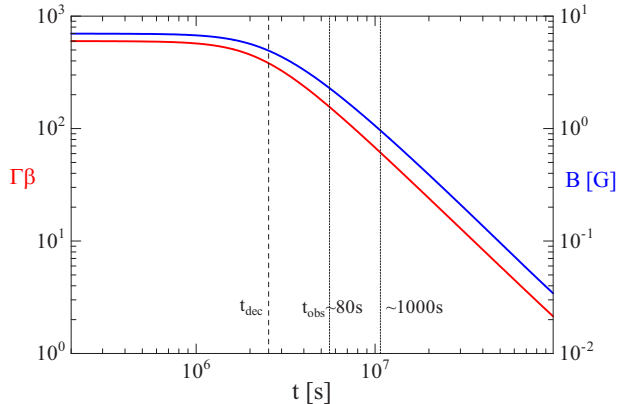


FIG. 1.— Evolutions of the bulk Lorentz factor (red, left axis) and the magnetic field (blue, right axis) for the ISM model. The time t is measured in the central engine rest frame. The vertical dashed line corresponds to the deceleration time, and the two vertical dotted lines indicate ~ 80 s and ~ 1000 s as the observation times on Earth.

decelerate, is

$$t_{\text{dec}} = \frac{1}{c} \left(\frac{3E_0}{4\pi n_0 m_p c^2 \Gamma_0^2} \right)^{1/3} \quad (9)$$

$$\simeq 2.5 \times 10^6 \left(\frac{E_0}{10^{54} \text{ erg}} \right)^{1/3} \left(\frac{n_0}{1 \text{ cm}^{-3}} \right)^{-1/3} \left(\frac{\Gamma_0}{600} \right)^{-2/3} \text{ s}. \quad (10)$$

The time t can be approximately transformed into the observer time as $t_{\text{obs}} = (1+z)t/(4\Gamma^2)$ (Sari et al. 1998), though the emission detected by an observer at a certain time is the superposition of photons emitted at different times from different latitudes. In Figure 1, we indicate the corresponding observer times of $t_{\text{obs}} = 80$ s and 1000 s by dotted lines. Most afterglow photons we discuss here are emitted between the two dotted lines.

The reverse-shock component is promptly added at $t = 4.9 \times 10^6$ s, which roughly corresponds to $t_{\text{obs}} = 50$ s, with the energy density of 0.7 erg cm^{-3} and the spectral peak energy 2.6×10^{-2} eV in the shell rest frame. Those parameters are chosen to reproduce the optical light curve (see Figure 3). While we cannot determine the spectral peak energy from the optical light curve alone, our choice well restricts the effect of this additional component to the optical range as shown in Figure 2. The injected photons gradually escape from the shell with a timescale of $t/(6\Gamma)$ in the shell rest frame. With the curvature effect on the dispersion of the photon arrival time, the resultant reverse-shock light curve shows a smooth behavior as shown in Figure 3.

Figure 2 shows the afterglow spectrum at $t_{\text{obs}} = 80$ s, when both MAGIC and *Fermi* detected signals. As mentioned above, the spectrum obtained with Method I deviates from the conventional broken power-law formula especially around the spectral peak. The obtained flux

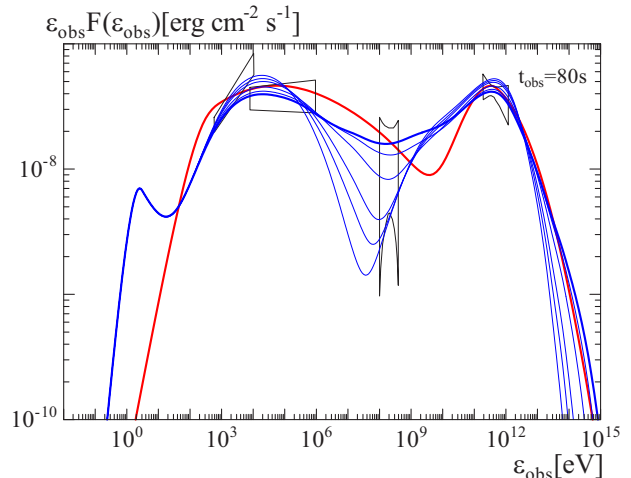


FIG. 2.— Model spectra at $t_{\text{obs}} = 80$ s for the ISM model. The observation data of *Swift* XRT and *Fermi* LAT are taken from Ajello et al. (2020), and the MAGIC data, which are corrected for attenuation caused by the extragalactic background light, is taken from MAGIC-MWL paper. We adopt the acceleration efficiency parameter $\eta = 1$ for the thick solid line. The blue lines are results with Method I, and the red line is obtained with Method II. The blue thin lines show model spectra with $\eta = 10, 100, 1000, 3000,$ and $10,000$, decreasing the 100 MeV flux (from top to bottom). The spectral peak at $\sim 1\text{--}10$ eV is the “reverse-shock” component we set manually.

is lower than the analytical formula in F17 by a factor of 2.3 and 1.6 at 10 keV and MeV, respectively. As the analytical formula neglects the inverse-Compton emission, those flux differences are not so large.

The thick line is the case with $\eta = 1$, which realizes the theoretically highest value of γ_{max} . In this case, the synchrotron emission by the electrons with a Lorentz factor close to γ_{max} is dominant in 0.1–1 GeV. The seed photons for the inverse-Compton component detected with MAGIC are dominated by the synchrotron photons from the forward shock, rather than the reverse-shock component at the optical energy range.

In Figure 2, we also plot the model spectrum (red line) obtained by Method II. The model parameters are shown in Table 1 as ISM (Method II). Although the curvature of the synchrotron spectrum around MeV is different from the spectrum obtained by the time-dependent code, we have obtained similar parameter sets as $f_e E_0 \sim 10^{53.5}$ erg, $f_e n_0 \sim 0.3$, $\epsilon_e/f_e \sim 0.1$, and $\epsilon_B/f_e \sim 10^{-3}$. Thus, our time-dependent results by F17 are supported by an independent calculation.

The multi-wavelength light curves are well reproduced as shown in Figure 3, although the initial 0.1–1 GeV emission for $t_{\text{obs}} \lesssim 10$ s, to which the prompt component can contribute, deviates from the model light curves. At $t_{\text{obs}} \sim 10^3$ s, the model fluxes of 0.3–1 TeV gamma-rays and X-rays are slightly brighter than the observed data. To reconcile those, we may need the evolutions of microscopic parameters in the framework of our model.

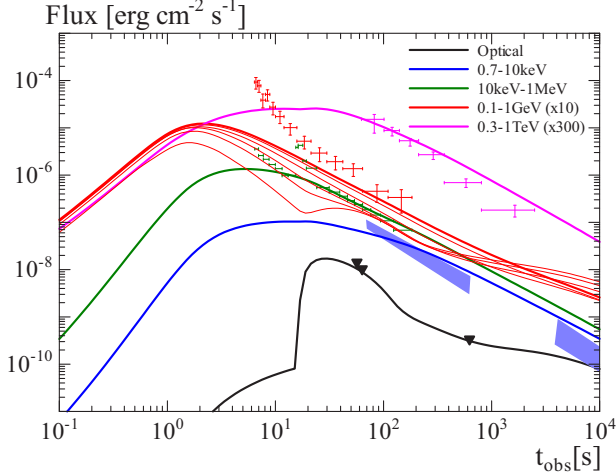


FIG. 3.— Model light curves for the ISM model. The observation data are taken from Ajello et al. (2020) (0.7–10 keV, 10 keV–1 MeV, 0.1–1 GeV) and MAGIC-MWL paper (optical, 0.3–1 TeV). The optical data are corrected for extinction due to the host and our Galaxy. The TeV gamma-ray data are also corrected for attenuation caused by the extragalactic background light. The thick lines show the model with $\eta = 1$. The red thin lines show the light curves for 0.1–1 GeV with $\eta = 10, 100, 1000, 3000,$ and $10,000$, decreasing the flux. The optical bump at ~ 20 – 100 s is the “reverse-shock” component we set manually.

A parameter set of higher ϵ_B but lower ϵ_e and f_e could realize the lower inverse-Compton flux maintaining the synchrotron flux at $t_{\text{obs}} \sim 10^3$ s.

As we decrease γ_{max} by increasing η (see thin blue lines in Figure 2), the 0.1–1 GeV emission is mostly coming from inverse-Compton emission. Since the error in the 0.1–1 GeV flux is large, a very large η seems acceptable from Figure 2. However, the hard spectra for $\eta \gtrsim 1000$ do not agree with the photon index ~ -2 reported in Ajello et al. (2020), and the energy-integrated fluxes in Figure 3 are inconsistent with the cases of $\eta \gtrsim 100$.

The ion skin depth characterized by the proton plasma frequency in the downstream is

$$c/\omega_{\text{pp}} = \sqrt{\frac{\Gamma m_p c^2}{4\pi e^2 (4\Gamma n_0)}} = \sqrt{\frac{m_p c^2}{16\pi e^2 n_0}} \quad (11)$$

$$\simeq 1.1 \times 10^7 \left(\frac{n_0}{1 \text{ cm}^{-3}}\right)^{-1/2} \text{ cm}, \quad (12)$$

which is independent of the bulk Lorentz factor Γ . The shortest wavelength mediated by the ion-Weibel instability can be expressed as $\lambda_{\text{min}} = \alpha c/\omega_{\text{pp}}$, where the dimensionless parameter $\alpha \sim 10$ (Ruyer & Fiuza 2018). The parameter η is inferred as $\sim r_L/\lambda_{\text{min}}$ by PIC simulations (Sironi et al. 2013). This factor is estimated for electrons with the maximum Lorentz factor by using Equation (3) and the expression of the acceleration time (see also Equation (1) of Ohira & Murase 2019) as

$$\eta_{\text{Weibel}} \approx \frac{1}{\Gamma} \frac{1}{(2m_p)^{\frac{5}{6}} \epsilon_B^{\frac{1}{2}}} \left(\frac{m_e}{\alpha}\right)^{\frac{2}{3}} \left(\frac{\pi}{n_0}\right)^{\frac{1}{6}} \left(\frac{3e}{c\sigma_T}\right)^{\frac{1}{3}} \quad (13)$$

$$\simeq 100 \left(\frac{\Gamma}{156}\right)^{-1} \left(\frac{\alpha}{7}\right)^{-\frac{2}{3}} \left(\frac{\epsilon_B}{9 \times 10^{-4}}\right)^{-\frac{1}{2}} \times \left(\frac{n_0}{1 \text{ cm}^{-3}}\right)^{-\frac{1}{6}}, \quad (14)$$

where $\Gamma = 156$ is the value at $t = 5.6 \times 10^6$ s ($t_{\text{obs}} \simeq 80$ s) in our simulation.

The value in Equation (14) is based on the analytical approximation. Given a value of η , our simulation directly provides the magnetic field, and γ_{max} obtained numerically: $B = 2.3$ G and $\gamma_{\text{max}} = 8.7 \times 10^7$ (7.8×10^6) for $\eta = 1$ (100) at $t = 5.6 \times 10^6$ s. The Larmor radius of the maximum-energy electrons is 6.5×10^{10} cm (5.8×10^9 cm) for $\eta = 1$ (100). We can obtain a value of η consistent with $\eta \sim r_L/\lambda_{\text{min}}$ adjusting the parameter α as

$$\eta \simeq 100 \left(\frac{\alpha}{5}\right)^{-1} \left(\frac{r_L}{5.8 \times 10^9 \text{ cm}}\right) \left(\frac{n_0}{1 \text{ cm}^{-3}}\right)^{1/2}. \quad (15)$$

The fiducial value of $\alpha \sim 10$ can barely realize the required limit $\eta \sim 100$ at the maximum energy, but to achieve the ideal value $\eta = 1$, a very large $\alpha \sim 5000$ is required. Note that the Larmor radius for $\gamma_m = 1.7 \times 10^4$ is comparable to the ion skin depth, namely shorter than λ_{min} for $\alpha \gtrsim 10$. The acceleration processes around γ_m and γ_{max} may be different, though we have assumed a single power-law injection.

Our parameter values of $\epsilon_e/f_e = 0.2$ and $\epsilon_B/f_e = 3 \times 10^{-3}$ are significantly larger than those in the afterglow model in MAGIC-MWL paper, $\epsilon_e/f_e = 0.07$ and $\epsilon_B/f_e = 8 \times 10^{-5}$. Adopting the simple analytical formulae for the spectral break energies neglecting the inverse-Compton cooling (see F17), the parameter set of the model in MAGIC-MWL paper provides $\epsilon_c \simeq 170$ keV $\gg \epsilon_m \simeq 60$ eV at $t_{\text{obs}} = 80$ s. Our numerical calculation with the same parameter set as that in MAGIC-MWL paper leads to a dimmer synchrotron flux than the observed one by a factor of ~ 10 . Even with the analytical formulae in F17, the MAGIC-MWL parameters yield $\epsilon_{\text{obs}} F(\epsilon_{\text{obs}}) \simeq 10^{-8}$ erg cm $^{-2}$ s $^{-1}$ at $\epsilon_{\text{obs}} = \text{MeV}$, which is lower than the observed flux by a factor of ~ 3 . Thus, we need to adopt larger values of ϵ_e/f_e and ϵ_B/f_e in our numerical method. Those requirements are similar for the results with Method II as well. In both of the methods, model fitting with $\epsilon_B/f_e \ll 10^{-3}$ is difficult to reproduce both the synchrotron and SSC fluxes.

The analytical estimate for our parameter set in F17 gives us $\epsilon_c \sim 3\epsilon_m \sim 2$ keV. The strong magnetic field leads to close values of ϵ_c and ϵ_m . Our numerical result shows a smoothly curved spectrum so that it is hard to identify the break energies of ϵ_m and ϵ_c . The synchrotron peak in Figure 2 is slightly higher than the analytical estimate of ϵ_c (see F17 for the detailed differences from the analytical formulae). To keep a high flux above ϵ_c , especially at GeV, a small index of $p < 2.5$ is required in our model.

Ajello et al. (2020) concluded that the X-ray spectral break (~ 5 keV) is due to ϵ_c . However, the analytical light curve for $\epsilon_m < \epsilon_{\text{obs}} < \epsilon_c$ is shallower ($\propto t^{3(1-p)/4}$) than the observed XRT light curve ($\propto t^{-1.3}$). Our X-ray light curve also shows a slightly shallower decay than the observed one.

4.2. Wind Model

Ajello et al. (2020) claimed that the wind model can reconcile the XRT light curve and the spectral-temporal closure relation at $\epsilon_m < \epsilon_{\text{obs}} < \epsilon_c$. However, the wind

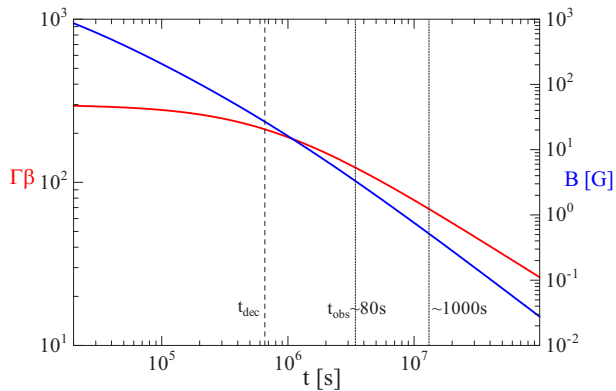


FIG. 4.— Evolutions of the bulk Lorentz factor (red, left axis) and the magnetic field (blue, right axis) for the wind model. The time t is measured in the central engine rest frame. The vertical dashed line corresponds to the deceleration time, and the two vertical dotted lines indicate ~ 80 s and ~ 1000 s as the observation time on earth, respectively.

model in MAGIC-MWL paper disagrees with the high flux of the early MAGIC light curve. Fraija et al. (2019) proposed a possible transition from wind-like medium to ISM-like medium at $t_{\text{obs}} = 300\text{--}400$ s. Here, we also test the wind model with our numerical code. The difference of flux from the analytical estimate is similar to the ISM case.

While a constant density was assumed in F17, we can simulate the afterglow in a wind-like circumstellar environment with the same numerical code adopting a density profile

$$n = 3.0 \times 10^{35} A R^{-2} \text{ cm}^{-3}, \quad (16)$$

where the dimensionless parameter A is interpreted by the mass-loss rate of the progenitor star as $10^{-5} A M_{\odot} \text{ yr}^{-1}$ with the wind velocity of 10^3 km s^{-1} . The evolutions of the bulk Lorentz factor Γ and the magnetic field B are shown in Figure 4. In the asymptotic region ($t \gtrsim 10^7$ s), the bulk Lorentz factor agrees with the analytical estimate of $\Gamma \propto t^{-0.5}$, while the magnetic field behaves as $B \propto t^{-1.4}$ slightly shallower than the analytical approximation $B \propto t^{-1.5}$. At the time corresponding to $t_{\text{obs}} \sim 80$ s, Γ deviates from the asymptotic power-law evolution, which slightly affects the light curve behavior.

At $t = 2.6 \times 10^6$ s, which corresponds to $t_{\text{obs}} \simeq 50$ s, we add the reverse-shock component with the energy density of 1.7 erg cm^{-3} and the peak energy of 2.1×10^{-2} eV in the shell rest frame. The spectral indices are the same as the ISM case.

As shown in Figure 5, we obtain similar spectra to those for the ISM model at $t_{\text{obs}} = 80$ s. The constraint for η for the wind model is also similar to that for the ISM model; $\eta \lesssim 100$ is required as shown in Figures 5 and 6. The combinations of the parameters $\epsilon_e/f_e = 0.27$ and $\epsilon_B/f_e = 4 \times 10^{-3}$ in our models are different from those for the wind model in MAGIC-MWL paper (0.6 and 10^{-4} , respectively). Similarly to the ISM model, the break energies of ϵ_m and ϵ_c reside in the X-ray band at $t_{\text{obs}} = 80$ s.

Even with the wind model, we obtain similar light curves to those in the ISM model. Contrary to expectation suggested by Ajello et al. (2020), the X-ray model light curve is shallower than the XRT light curve for

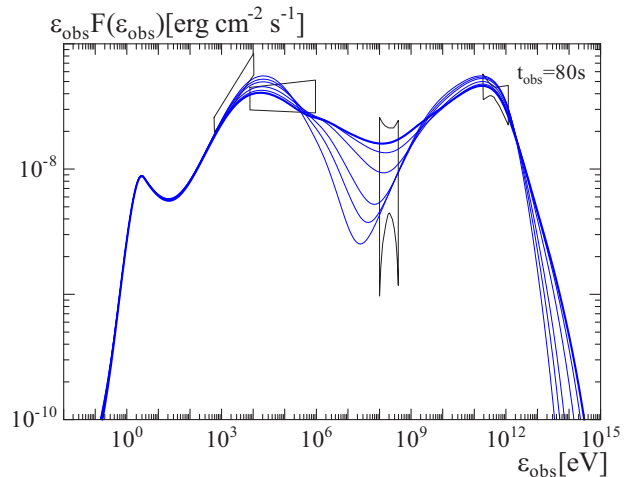


FIG. 5.— Model spectra at $t_{\text{obs}} = 80$ s for the wind model. We adopt the acceleration efficiency parameter $\eta = 1$ for the thick solid line. The thin lines show model spectra with $\eta = 10, 100, 1000, 3000,$ and $10,000$, decreasing the 100 MeV flux (from top to bottom). The spectral peak at $\sim 1\text{--}10$ eV is the “reverse-shock” component we set manually.

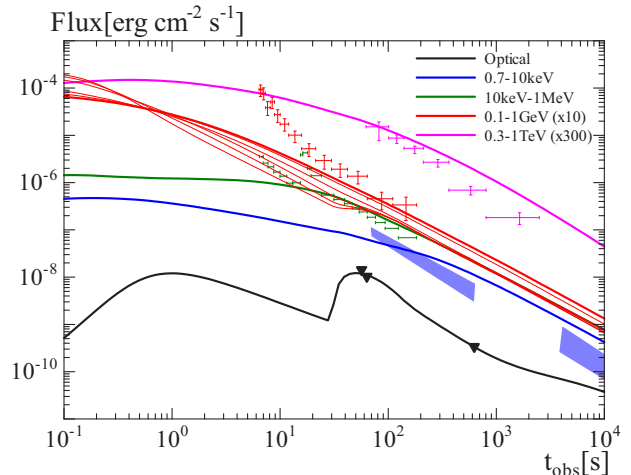


FIG. 6.— Model light curves for the wind model. The thick lines show the model with $\eta = 1$. The red thin lines show the light curves for 0.1–1 GeV with $\eta = 10, 100, 1000, 3000,$ and $10,000$, decreasing the flux. The optical bump at $\sim 20\text{--}100$ s is the “reverse-shock” component we set manually.

$t_{\text{obs}} < 10^3$. In our parameter set, the X-ray (~ 0.7 keV) energy range is still below $\epsilon_m (< \epsilon_c)$, where the flux is supposed to be constant in the analytical formula. The early optical bump at $t_{\text{obs}} \sim 1$ s in Figure 6 is originated from synchrotron emission from secondary electron–positron pairs injected due to very high-density environment in the very early epoch.

In both the ISM and wind models, the magnetic field and Lorentz factor at the time corresponding to $t_{\text{obs}} \simeq 80$ s are similarly a few G and ~ 100 , respectively (see Figures 1 and 4). We can expect that those values do not largely depend on models, though ϵ_B itself is not strongly constrained because of the uncertainty in f_e .

5. THERMAL SYNCHROTRON EMISSION

If a fraction of electrons are not injected into the acceleration process (i.e., $f_e < 1$), such “thermal” electrons also emit synchrotron photons. Eichler & Waxman (2005) pointed out that the thermal synchrotron emis-

sion is expected in the radio wavelength at the early phase (see also Warren et al. 2017, 2018), and it is naturally expected for non-relativistic or trans-relativistic shocks Samuelsson et al. (2020). However, the early-phase ($t \lesssim 10^2$ s) radio observation is challenging mission. Toma et al. (2008) argued that the Faraday depolarization effect by the thermal electrons can be probed by the late-phase polarimetric observations at the radio frequencies above the synchrotron self-absorption frequency. The relatively low polarization ($\sim 0.3\%$) of the GRB 171205A afterglow in the millimeter and submillimeter ranges may imply $f_e \sim 0.1$ (Urata et al. 2019), though it is difficult to set a robust lower-limit for f_e . While the radio observations have been focused in this issue, Ressler & Laskar (2017) claimed that early X-ray and optical afterglow could be dominated by the thermal synchrotron component.

Here we discuss an alternative interpretation with the early thermal synchrotron signal for GRB 190114C. If f_e is small enough, the early optical emission can be interpreted as the thermal synchrotron emission rather than the reverse-shock component as shown below.

Given the evolution of the bulk Lorentz factor as shown in Figure 1 or 4, we can estimate the density of the thermal electrons $n_{\text{th}} = (1 - f_e)n_{\text{sh}}$, where

$$n_{\text{sh}} \approx 4\Gamma n, \quad (17)$$

and their temperature T from the energy density,

$$3Tn_{\text{th}} = \Gamma \left(1 + \epsilon_{\text{th}} \frac{m_{\text{p}}}{m_{\text{e}}} \right) n_{\text{th}} m_{\text{e}} c^2. \quad (18)$$

Here we have introduced a parameter ϵ_{th} , the fraction of the energy transferred from protons to thermal electrons. Several PIC simulations of relativistic shocks (e.g., Spitkovsky 2008; Sironi & Spitkovsky 2011; Kumar et al. 2015) have shown that the ion-Weibel instability significantly heats incoming electrons in the upstream. The thermal electron energy density in the downstream reach the nearly equipartition with the ion energy density, so that we can expect $\epsilon_{\text{th}} \sim 0.1\text{--}0.5$ according to those simulations. A fraction of electrons are reflected at the shock entering the Fermi acceleration process. The simulations by Sironi & Spitkovsky (2011) with $\Gamma = 15$ are consistent with $f_e \sim 0.02$ and $\epsilon_e \sim 0.1$.

Given the uniform intensity $I_0(\varepsilon)$ at a stationary surface of radius R , the luminosity is calculated as $L_0(\varepsilon) = 4\pi^2 R^2 I_0(\varepsilon)$. If this surface is relativistically expanding with a Lorentz factor Γ , the solid angle an observer can see is $\Omega \approx \pi(R/\Gamma D_{\text{A}})^2$ because of the relativistic beaming effect, where $D_{\text{A}} = D_{\text{L}}/(1+z)$ is the angular diameter distance. Using the luminosity distance D_{L} and the transformation

$$I(\varepsilon) \approx \left(\frac{\Gamma}{1+z} \right)^3 I_0(\varepsilon_0), \quad (19)$$

within this solid angle, we obtain the spectral flux for an observer as

$$F_{\text{obs}}(\varepsilon) \approx I(\varepsilon)\Omega \approx \frac{\Gamma(1+z)}{4\pi D_{\text{L}}^2} L_0(\varepsilon_0), \quad (20)$$

where $\varepsilon_0 = (1+z)\varepsilon/\Gamma$.

With the effect of synchrotron self-absorption, the intensity of the thermal synchrotron emission is written as

$$I_{\text{th}}(\varepsilon) = \frac{2\varepsilon^2 T}{c^2 h^3} \left(1 - e^{-\tau(\varepsilon)} \right), \quad (21)$$

where $\tau(\varepsilon) = \alpha(\varepsilon)\Delta R$ is the optical depth. In a thermal plasma, the absorption coefficient is

$$\alpha(\varepsilon) = \frac{j_{\text{th}}(\varepsilon)c^2 h^3}{2\varepsilon^2 T}, \quad (22)$$

where $j_{\text{th}}(\varepsilon)$ is the thermal synchrotron emissivity calculated from the magnetic field and the electron energy distribution

$$\frac{dn_{\text{th}}}{d\varepsilon_e} = \frac{n_{\text{th}}}{2T^3} \varepsilon_e^2 \exp(-\varepsilon_e/T). \quad (23)$$

The single-zone approximation with particle number conservation provides us the shell width in the shell rest frame as $\Delta R = R/(12\Gamma)$ and $R/(4\Gamma)$ for the ISM and wind cases, respectively. Finally we obtain the thermal synchrotron flux for an observer as

$$F_{\text{th}}(\varepsilon) \approx \pi \frac{(1+z)^3}{\Gamma} \left(\frac{R}{D_{\text{L}}} \right)^2 \frac{2\varepsilon^2 T}{c^2 h^3} \left(1 - e^{-\tau(\varepsilon_0)} \right). \quad (24)$$

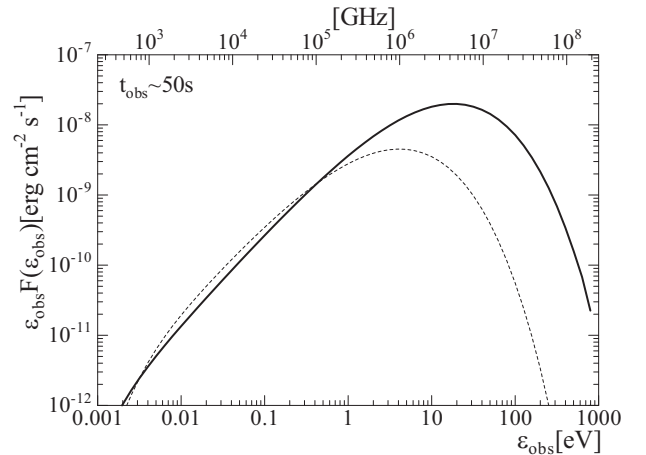


FIG. 7.— Model spectra for the thermal synchrotron emission at $t_{\text{obs}} \sim 50$ s in the ISM model. The evolutions of the Lorentz factor Γ and magnetic field B are the same as those in Figure 1. We fix $f_e = 0.01$, and adopt $\epsilon_{\text{th}} = 0$ (solid) and 6×10^{-4} (dashed), respectively.

Given the Lorentz factor and magnetic field (see Figure 1), Equation (24) provides us the thermal synchrotron spectrum at an arbitrary time $t_{\text{obs}} = (1+z)t/(4\Gamma^2)$ as shown in Figure 7. To make the thermal synchrotron flux comparable to the observed optical flux, we need $f_e \lesssim 0.01$, namely the number density of the thermal electrons is required to be more than 100 times the non-thermal electron density. The synchrotron self-absorption frequency in the examples in Figure 7 is \sim THz, so that the polarization in radio band typically below 100 GHz should be greatly suppressed in those parameter sets. In Figure 8, we plot the thermal synchrotron light curves with $f_e = 0.01$. Even with a small value of $\epsilon_{\text{th}} < 10^{-3}$, the thermal emission can reproduce

the optical flux at $t_{\text{obs}} = 50\text{--}60$ s without the reverse-shock component.

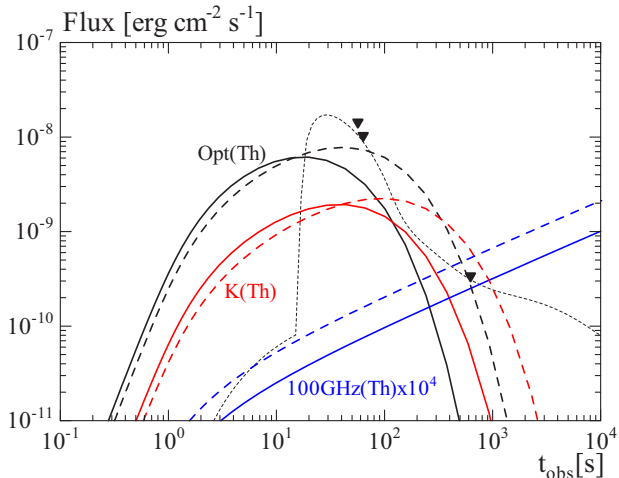


FIG. 8.— Model light curves for the thermal synchrotron emission in the ISM model. The evolutions of the Lorentz factor Γ and magnetic field B are the same as those in Figure 1. The black thin dashed line is the same non-thermal model for the optical band in Figure 3. The thermal optical (black), infrared (K band, red), and radio (100 GHz, blue) are plotted. We fix $f_e = 0.01$, and adopt $\epsilon_{\text{th}} = 0$ (solid) and 6×10^{-4} (dashed), respectively.

The characteristic point in the thermal model is the light curve crossing for the optical and infrared bands at $t_{\text{obs}} \sim 100$ s (300 s) for $\epsilon_{\text{th}} = 0$ (6×10^{-4}). Such behavior is hard to be realized by non-thermal emission mechanisms.

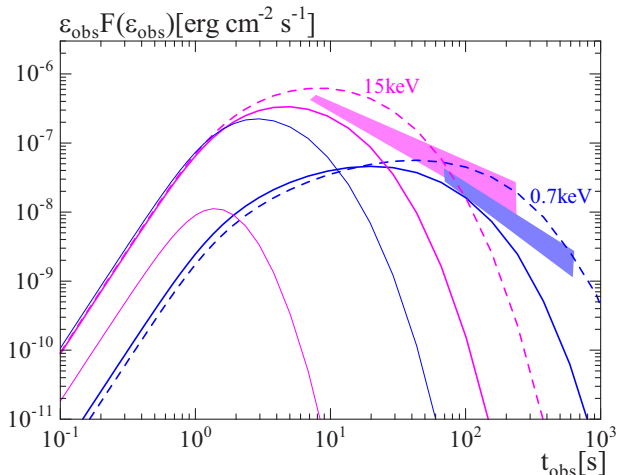


FIG. 9.— X-ray Model light curves for the thermal synchrotron emission in the ISM model. The non-thermal X-ray fluxes ($\epsilon_{\text{obs}} F(\epsilon_{\text{obs}})$, shaded regions) at 0.7 keV (blue) and 15 keV (magenta) are estimated from the data in Ajello et al. (2020) assuming $\epsilon_{\text{obs}} F(\epsilon_{\text{obs}}) \propto \epsilon_{\text{obs}}^0$. The evolutions of the Lorentz factor Γ and magnetic field B are the same as those in Figure 1. The thermal synchrotron emission at 0.7 keV (blue) and 15 keV (magenta) are plotted with parameter values of $f_e = 0.01$ & $\epsilon_{\text{th}} = 6 \times 10^{-4}$ (thin solid), $f_e = 0.3$ & $\epsilon_{\text{th}} = 0.01$ (thick solid), and $f_e = 0.3$ & $\epsilon_{\text{th}} = 0.02$ (thick dashed).

The value $f_e = 0.01$ requires a very large energy $E_0 = 3 \times 10^{55}$ erg, which can be regarded as a caveat of the interpretation by synchrotron emission from thermal electrons. Even assuming a reasonable value of $f_e = 0.3$,

we can constrain the parameter value of ϵ_{th} from the early X-ray light curves.

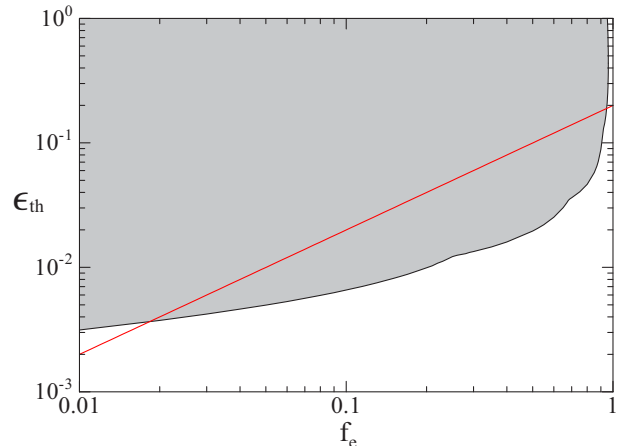


FIG. 10.— The upper limits of ϵ_{th} in the ISM model. The parameter sets in the gray shaded region yield a brighter X-ray flux than observed. The red line shows the value of $\epsilon_e = 0.06$ ($f_e/0.3$) in our model.

Changing the value of f_e , we obtain the upper limit of ϵ_{th} from the constraints by the 0.7 keV and 15 keV light curves. The result is shown in Figure 10. For a finite value of $1 - f_e$, a value of ϵ_{th} larger than 10^{-2} is unlikely. Only the case of $f_e \simeq 1$ is acceptable for $\epsilon_{\text{th}} \gtrsim 10^{-2}$. The small ϵ_{th} does not agree with the present PIC simulations of relativistic shocks. Our results imply that the temperature of the thermal electrons should be not much larger than $\Gamma m_e c^2$ if a dominant fraction of electrons remains thermal. Some additional effects to make the thermal electrons reenter the Fermi acceleration process are required, which increases the non-thermal fraction or makes all electrons be non-thermal population (i.e., $f_e \simeq 1$).

In the wind model, the stronger magnetic field in the early stage gives a more stringent upper limit for ϵ_{th} than that in Figure 10.

6. SUMMARY AND DISCUSSION

The inverse-Compton component detected with MAGIC telescopes from GRB 190114C uniquely constrains the magnetic field and non-thermal electron population at the early phase of the afterglow. In this paper, using our time-dependent code (Method I) provided by F17, we reproduced the broadband spectrum and light curves of the early afterglow of GRB 190114C. The flux ratio of the inverse-Compton component to the synchrotron component at $t_{\text{obs}} \simeq 80$ s is consistent with the models with microscopic parameters of $\epsilon_e/f_e \sim 0.1$ and $\epsilon_B/f_e \sim 10^{-3}$, irrespective of the models of the circumstellar environment (ISM or wind). The independent numerical code (Method II) also provides a result consistent with $\epsilon_B/f_e \sim 10^{-3}$. The required magnetic field and Lorentz factor are a few gauss and ~ 100 , respectively, at the time corresponding to $t_{\text{obs}} \simeq 80$ s.

However, the observed decay index of the X-ray afterglow is slightly steeper than the model light curves. The spectra shown in Ajello et al. (2020) do not show a significant evolution of the break energy (~ 5 keV) from $t_{\text{obs}} = 68$ s to 627 s, which does not agree with both

the standard ISM and wind models for both the fast ($\varepsilon_c < \varepsilon_m$) and slow ($\varepsilon_m < \varepsilon_c$) cooling cases. Although this unexpected behavior of the break energy may require the time evolution of the microscopic parameters even for this time interval, the strength of the magnetic field can be expected not far different from our estimate at least at $t_{\text{obs}} \simeq 80$ s (see §3).

The flux detected with *Fermi* above 0.1 GeV constrains the acceleration efficiency parameter as $\eta \lesssim 100$, which adjusts the maximum electron Lorentz factor γ_{max} . The acceleration timescale is required shorter than $100/(2\pi) \sim 20$ times the gyroperiod. The simple estimate $\eta \sim \gamma_{\text{max}} m_e c \omega_{\text{pp}} / (10eB)$ supported by the state-of-art PIC simulations seems to be marginally consistent with $\eta \sim 100$. If the actual η is much smaller, the maximum energy of non-thermal electrons would need to be regulated by another mechanism rather than the diffusive process seen in the early stage of the Fermi acceleration in the PIC simulations. For example, a large-scale MHD turbulence may play an important role in acceleration of the highest-energy electrons (Zhang et al. 2009; Inoue et al. 2011; Demidem et al. 2018; Teraki & Asano 2019). Note that the Larmor radius of electrons of γ_m may be shorter than the coherence length scale λ_{min} of turbulence required to make η small enough. This implies a different acceleration process for such low-energy electrons. The entire particle-acceleration mechanism at relativistic shocks may be a compound one.

It is natural that only a fraction of electrons are ac-

celerated by the shock and the rest of electrons remain as the thermal component, which is especially the case for mildly relativistic shocks. The early optical and X-ray afterglow emissions constrain the non-thermal fraction f_e and the heating efficiency ϵ_{th} of the thermal electrons. Intriguingly, we found that the thermal synchrotron model with $f_e = 0.01$ and $\epsilon_{\text{th}} = 6 \times 10^{-4}$ can explain the early optical emission instead of the reverse-shock emission, although the required total energy becomes as large as $E_0 = 3 \times 10^{55}$ erg. This model predicts a characteristic behavior of light curves – light curve crossing for the optical and infrared bands. However, this interpretation would contradict with the results of the PIC simulations for ultra-relativistic shocks. The PIC simulations have shown fairly large values of ϵ_{th} , i.e., a significant fraction of electrons are heated. In this case, if $f_e \ll 1$, the thermal X-ray emission should contribute to the early afterglow. The absence of such a component in the X-ray light curves rules out values $\epsilon_{\text{th}} \gtrsim 10^{-2}$ or indicates $f_e \simeq 1$. Those results provide us important clue to probing plasma physics with relativistic shocks.

We acknowledge useful suggestions by the anonymous referee. This work is supported by the joint research program of the Institute for Cosmic Ray Research (ICRR), the University of Tokyo. The work of K.M. is supported by the Fermi GI program 111180, and NSF grant No. AST-1908689. This work is also supported by JSPS KAKENHI Grant No. 20H01901 (K.M.) and No. 18H01245 (K.T.).

REFERENCES

- Ackermann, M., Ajello, M., Asano, K., et al. 2014, *Science*, 343, 42
- Ajello, M., Arimoto, M., Axelsson, M., et al. 2020, *ApJ*, 890, 9
- Band, D., Matteson, J., Ford, L., et al. 1993, *ApJ*, 413, 281
- Blandford, R. D., & Mckee, C. F. 1976, *PhFl*, 19, 1130
- Chen, X., Fossati, G., Liang, E. P., & Böttcher, M. 2011, *MNRAS*, 416, 2368
- Demidem, C., Lemoine, M., & Casse, F. 2018, *MNRAS*, 475, 2713
- Derishev, E., & Piran, T. 2019, *ApJ*, 880, L27
- Eichler, D., & Waxman, E. 2005, *ApJ*, 627, 861
- Fraija, N., Barniol Duran, R., Dichiara, S., & Beniamini, P. 2019, *ApJ*, 883, 162
- Fraija, N., Dichiara, S., Pedreira, A. C., et al. 2019, *ApJ*, 879, L26
- Fukushima, T., To, S., Asano, K., & Fujita, Y. 2017, *ApJ*, 844, 92 (F17)
- Inoue, T., Asano, K., & Ioka, K. 2011, *ApJ*, 734, 77
- Ioka, K., Toma, K., Yamazaki, R., & Nakamura, T. 2009, *A&A*, 458, 7
- Kangas, T., & Fruchter, A. S. 2019, arXiv:1911.01938
- Kumar, R., Eichler, D., & Gedalin, M. 2015, *ApJ*, 806, 165
- Lemoine, M., & Pelletier, G. 2011, *MNRAS*, 417, 1148
- MAGIC Collaboration 2019, *Nature*, 575, 455
- MAGIC Collaboration, et al. 2019, *Nature*, 575, 459 (MAGIC-MWL)
- Maselli, A., Melandri, A., Nava, L., et al. 2014, *Science*, 343, 48
- Mészáros, P. & Rees, M. J. 1997, *ApJ*, 476, 232
- Misra, K., Resmi, L., Kann, D. A., et al. 2019, arXiv:1911.09719
- Murase, K., Toma, K., Yamazaki, R., & Mészáros, P. 2011, *ApJ*, 732, 77 (M11)
- Ohira, Y., & Murase, K. 2019, *Phys. Rev. D*, 100, 061301(R)
- Panaitescu, A., & Kumar, P. 2001, *ApJ*, 554, 667
- Ressler, S. M., & Laskar, T. 2017, *ApJ*, 845, 150
- Ruyer, C., & Fiuzza, F. 2018, *Phys. Rev. Lett.*, 120, 245002
- Samuelsson F., Bégué D., Ryde F., Pe’er A., Murase K., 2020, *ApJ*, 902, 148
- Sari, R., Piran, T., & Narayan, R., 1998, *ApJ*, 497, L17
- Sironi, L., & Spitkovsky, A. 2011, *ApJ*, 726, 75
- Sironi, L., Spitkovsky, A., & Arons, J. 2013, *ApJ*, 771, 54
- Spitkovsky, A. 2008, *ApJ*, 673, L39
- Teraki, Y., & Asano, K. 2019, *ApJ*, 877, 71
- Toma, K., Ioka, K., & Nakamura, T. 2008, *ApJ*, 673, L123
- Urata, Y., Toma, K., Huang, K., Asada K., Nagai, H., Takahashi, S., Petitpas, G., Tashiro, M., & Yamaoka, K. 2019, *ApJ*, 884, L58
- Wang, X.-Y., Liu, R.-Y., Zhang, H.-M., Xi, S.-Q., & Zhang, B. 2019, *ApJ*, 884, 117
- Warren, D. C., Ellison, D. C., Barkov, M. V., & Nagataki, S. 2017, *ApJ*, 835, 248
- Warren, D. C., Barkov, M. V., Ito, H., Nagataki, S., & Laskar, T. 2018, *MNRAS*, 480, 4060
- Zhang, H., Christie, I. M., Petropoulou, M., Rueda-Becerril, J. M., & Giannios, D. 2020, *MNRAS*, 496, 974
- Zhang, B., Murase, K., Yuan, C., Kimura, S. S., & Mészáros, P. 2020b, in preparation
- Zhang, W., MacFadyen, A., & Wang, P. 2009, *ApJ*, 692, 240